iScience

CellPress

Article

Biomechanical Design of the Mantis Shrimp Saddle: A Biomineralized Spring Used for Rapid Raptorial Strikes

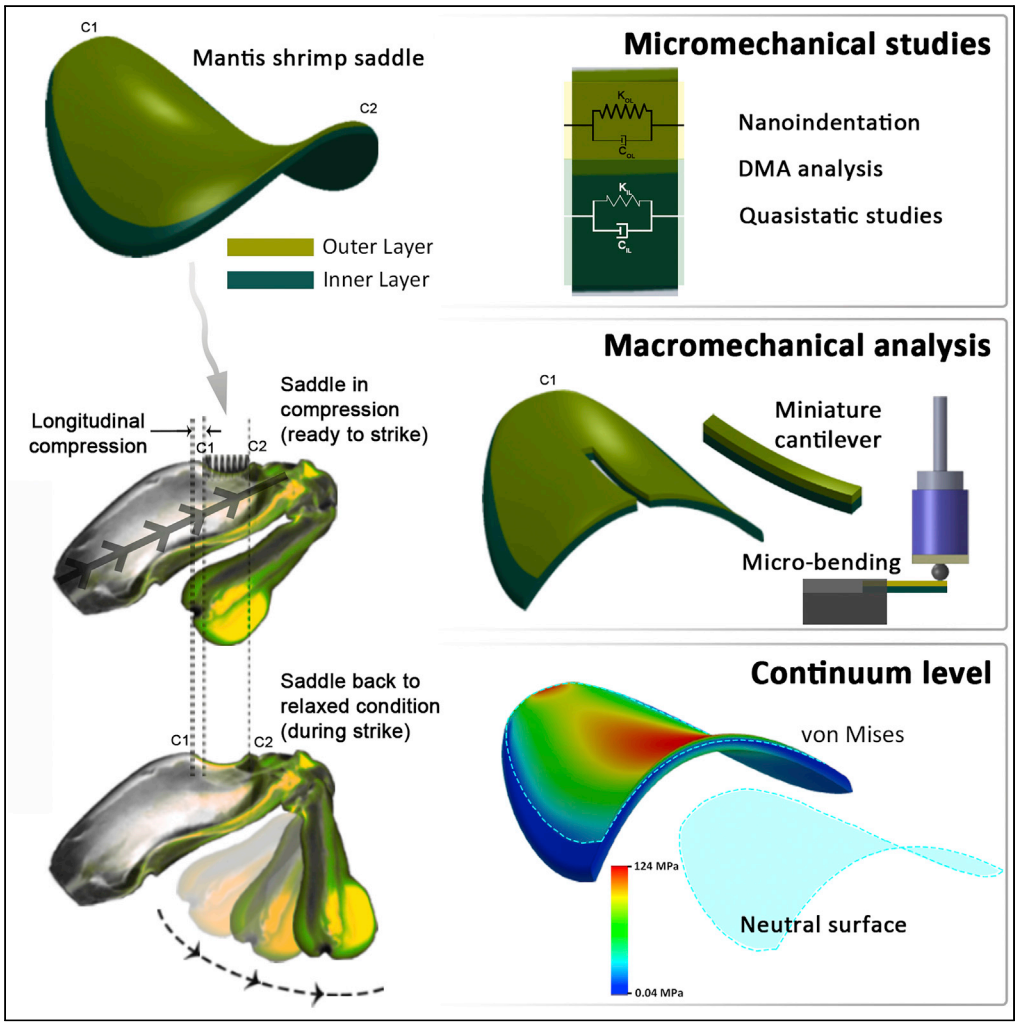

Maryam Tadayon, Shahrouz Amini, Zhongke Wang, Ali Miserez

ali.miserez@ntu.edu.sg

HIGHLIGHTS

Mantis shrimp delivers one of the most powerful strikes in the animal kingdom

During a strike, the elastic energy is stored in a saddle-shaped mineralized spring

The saddle is a bilayer structure with optimized distribution of components

The biomechanical design of the saddle ensures efficient storage of elastic energy

Tadayon et al., iScience *8*, 271–282
October 26, 2018
https://doi.org/10.1016/j.isci.2018.08.022

iScience

CellPress

Article

Biomechanical Design of the Mantis Shrimp Saddle: A Biomineralized Spring Used for Rapid Raptorial Strikes

Maryam Tadayon,[1,4] Shahrouz Amini,[1,4] Zhongke Wang,[2] and Ali Miserez[1,3,5,*]

SUMMARY

Stomatopods deliver one of the fastest strikes in the animal kingdom using their powerful "dactyl clubs." This kinematic performance is enabled by a power amplification device whereby elastic energy is stored in a saddle-shape mineralized bilayer structure. We combined a set of comprehensive micro-mechanical measurements with finite element modeling (FEM) to quantitatively elucidate the saddle biomechanical design. Dynamic nano-scale testing reveals that viscoelastic dissipation is minimized in the highly mineralized layer, whereas micro-bending experiments on miniature cantilevers highlight the critical role of the bilayer arrangement in optimizing storage of elastic energy. FEM shows that the saddle shape prevents stress concentration and the stresses remain well within the elastic range during loading, while the neutral surface coincides with the bilayer interface to prevent interfacial delamination. The study unveils the multi-scale design behind the intriguing ability of the saddle to store a high density of elastic energy using stiff but intrinsically brittle materials.

INTRODUCTION

Swift kinematic motions are critical evolutionary features in many biological systems, notably for escape or predatory strategies. From small insects such as the trap-jaw ant that quickly closes its mandibles for body propulsion (Patek et al., 2006), to the powerful strikes of crocodile jaws (Erickson et al., 2014), to the venus flytrap mechanism used to capture insects (Forterre et al., 2005), nature has evolved a diverse range of ultra-fast movements. A salient example that has received prominent interest in recent years is the powerful strike of the stomatopod (commonly called the mantis shrimp) dactyl club (Patek et al., 2004) (Figure 1). Stomatopods are aggressive crustaceans that deploy their pair of dactyl clubs as ultra-fast, hammer-like weapons to strike preys at velocities as high as 23 m/s (Patek et al., 2004), generating high-load impact forces against both soft and hard bodies.

Muscles alone are not enough to provide the required input energy released during a strike. Thus stomatopods have evolved a saddle-shape spring acting as a power amplification system (deVries et al., 2012; Patek and Caldwell, 2005; Patek et al., 2007) (Figures 1A and 1B). Input energy comes from the muscles and connective tissues, which slowly and elastically load the saddle spring (in a quasi-static mechanism), and the release of the elastic stored energy provides acceleration and power to the dactyl club during striking (Figure 1C) (Patek et al., 2007). An ideal spring should be both stiff and extensible to maximize storage of elastic energy, but this brings an inherent material limitation because these characteristics are usually mutually exclusive from a fracture mechanics perspective (Ritchie, 2011; Lawn, 1993). In a recent study, we discovered that to overcome this limitation, stomatopods have evolved their saddle as a bilayer structure at the meso-scale, which is built from a multi-phase biocomposite at the micro-scale with optimized organic/inorganic ratios within each layer (Figures 1D and 1E). The outer layer, subjected to compressive stresses during loading, is heavily mineralized, whereas the inner layer, sustaining tensile stresses, contains a higher content of biopolymeric phases (Tadayon et al., 2015). We postulated that this design allows the optimum storage of elastic energy while at the same time impeding brittle failure. Indeed, the layer subjected to tensile stresses is predominantly composed of tensile-resistant biopolymers, whereas the strongly mineralized layer is subjected to compressive stresses, thus in principle precluding premature fracture since minerals (including biominerals) are much less brittle in compression (Meyers et al., 2006).

However, a quantitative analysis of the saddle mechanical design is still lacking and it remains elusive how the spatial phase distribution and bilayer organization translate into the macroscopic response at the

[1]Biological and Biomimetic Materials Laboratory, School of Materials Science and Engineering, Nanyang Technological University, Singapore 637553, Singapore

[2]Singapore Institute of Manufacturing Technology (SIMTECH), Agency for Science, Technology, and Research (A*Star), Singapore 638075, Singapore

[3]School of Biological Sciences, Nanyang Technological University, 60 Nanyang Drive, Singapore 637551, Singapore

[4]Present address: Department of Biomaterials, Max Planck Institute of Colloids and Interfaces, Potsdam-Golm 14476, Germany

[5]Lead Contact

*Correspondence: ali.miserez@ntu.edu.sg

https://doi.org/10.1016/j.isci.2018.08.022

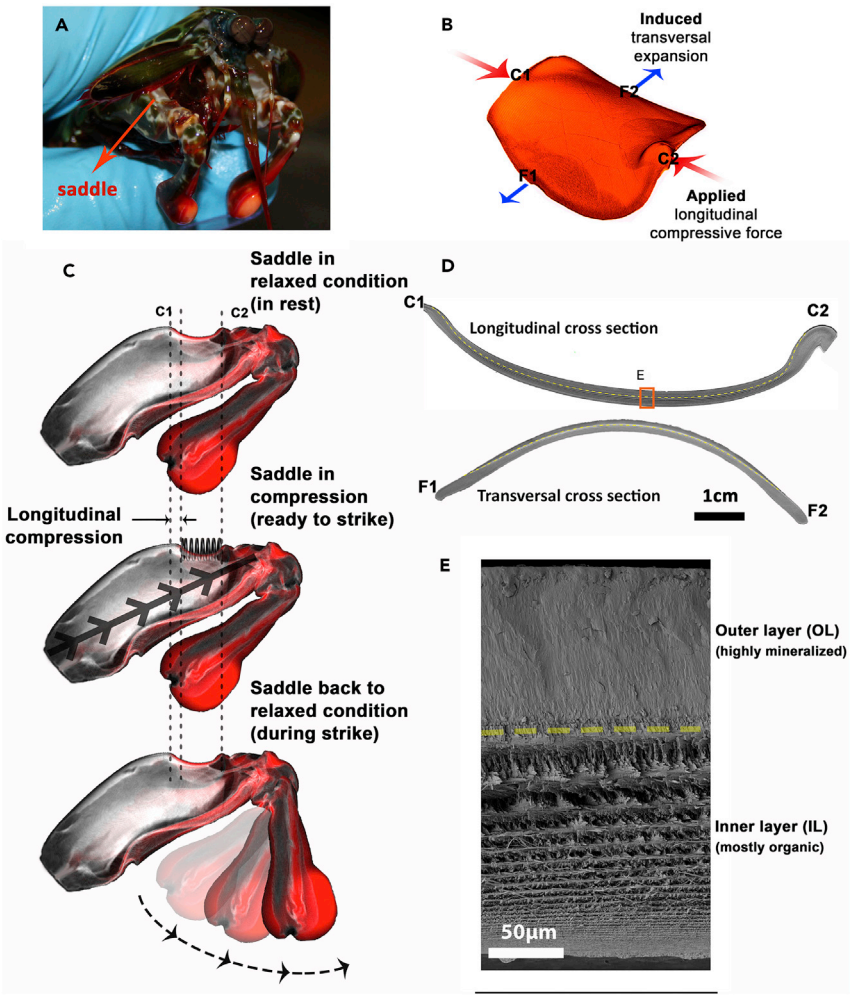

Figure 1. Saddle Structure of the *Odontodactylus scyllarus* (Peacock Mantis Shrimp)

(A) Location of the saddle in the animal.

(B) MicroCT image of the appendage used to illustrate the spring functionality of the saddle.

(C) MicroCT image of the combined saddle and dactyl club, illustrating the three loading stages of a strike: resting position (top), compressed position right before striking (middle), and relaxed state again (bottom) after strike.

(D) Field emission scanning electron micrograph of the saddle in longitudinal and transversal cross-sections adapted after Tadayon et al. (2015). The dashed line depicts the interface between the outer layer (OL) and the inner layer (IL). C1 and C2 are the contact points attached to the hard shell. F1 and F2 are the free edges that are connected to a soft membrane in the animal.

(E) Higher magnification field emission scanning electron microscopy (SEM) micrograph of a fractured surface of a saddle, showing the distinct microstructure within each layer. The micrograph corresponds to the orange box shown in panel D.

continuum level. In addition, conclusive experimental confirmation that the bilayer design maximizes storage of elastic energy with minimal viscoelastic dissipation remains to be established. In this study, we sought to answer these fundamental questions both experimentally and numerically. We designed specific micro- and nano-mechanical experiments to extract the elastic-plastic properties and the viscoelastic dissipation of the individual layers, the tensile curves of the biopolymeric phases, as well as the bending response of the bilayer using miniature cantilevers extracted from the saddle by picosecond laser machining. All experimental data were input into FEM of the whole saddle. Our findings demonstrate that the saddle design—mineral-dominated layer loaded in compression and biopolymer-dominated layer loaded in tension—indeed leads to a high elastic storage capacity, with minimal viscoelastic dissipation in the highly mineralized layer. Furthermore, FEM quantitatively establishes that the saddle geometry and phase distribution confer high safety factors: during saddle loading, maximum stresses within each layer

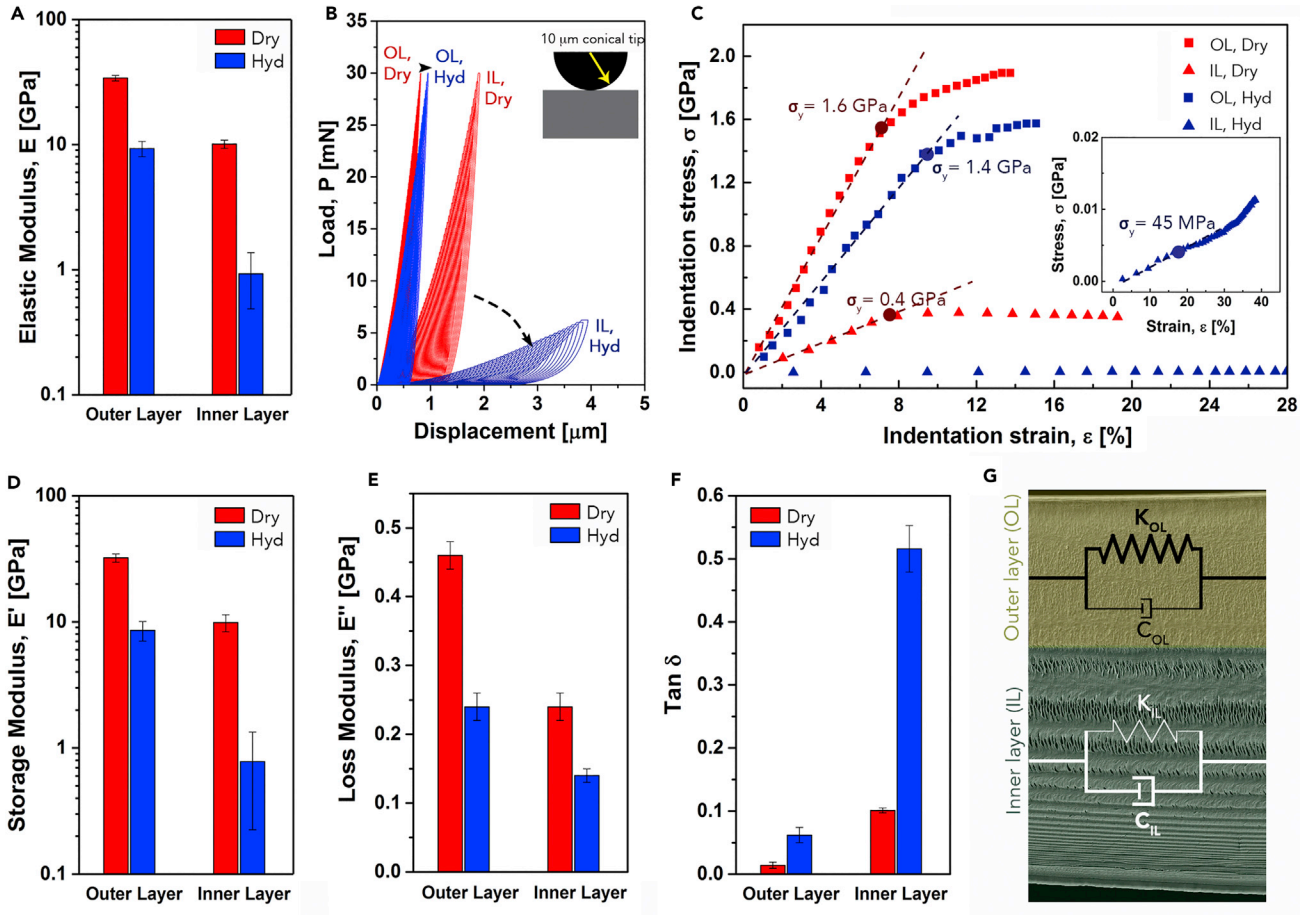

Figure 2. Mechanical Properties of Each Layer by Static Hertzian Nano-Contact Mechanics Measurements and by Dynamic Nano-Mechanical (DMA) Analysis. All error bars in the plots represent SDs.

(A) The elastic modulus of the OL is 3 and 5 times higher than that of the IL in dry (red) and hydrated (blue) conditions, respectively.

(B) Partial loading-unloading indentation curves on two different layers in dry and hydrated (hyd) conditions using a 10 μm cono-spherical tip.

(C) Elastic-plastic response of each layer in terms of indentation stress-strain curves in both dry and hydrated conditions. The curves were obtained from the partial loading-unloading cyclic experiments shown in (B).

(D–F) (D) Storage modulus, (E) loss modulus, and (F) damping coefficient (tan δ) of each layer in dry and hydrated conditions.

(G) Illustration of the viscoelastic response of the individual layers based on Kelvin-Voigt's model. The outer layer has a stiffer spring (K_{OL}) and minimal viscous loss (represented by the dashpot, C_{OL}), whereas the situation is opposite for the inner layer (K_{OL} and C_{IL}). The underlying image is a SEM micrograph.

remain in the elastic regime and well below the yield strength of the constitutive materials, thus ensuring that mantis shrimps can safely load their saddle hundreds of times for striking without inducing internal fatigue damage.

RESULTS

Micro-Mechanical Response of the Individual Layers

Recent investigations (Tadayon et al., 2015) have revealed the overall material property design of the saddle at the micro-scale, which is essentially a bilayer structure with a high mechanical contrast between the layers. The outer layer is predominantly mineralized and made of amorphous calcium carbonate, with an elastic modulus E of *ca.* 34 GPa in dry conditions, that decreases to *ca.* 10 GPa in hydrated conditions. The inner layer has a higher organic fraction, resulting in a lower elastic modulus of *ca.* 10 GPa in the dry state. Owing to the high biopolymeric content, the elastic modulus of the inner layer displays a sharper decay in the hydrated state with a modulus of *ca.* 0.9 GPa (Figure 2A). For quantitative design analysis of the saddle mechanics, additional experimental parameters of the individual layers are necessary. First, the yield strength (σ_y) of the individual layers is a critical design parameter, since it informs us on the upper

stress level above which irreversible damage would occur. Second, the dynamic mechanical response is important to assess the viscoelastic loss. And third, since the inner mesoscopic layer is subjected to tensile loading, its stress-strain response in tension is more representative of the actual loading regime in the native structure. These experimental parameters were obtained using the nano- and micro-mechanics experiments described below.

Elastic-Plastic Properties by Nano-Contact Mechanics Measurements

To assess the layer-specific yield strength, we conducted Hertzian contact mechanics measurements at the nano-scale, allowing us to acquire the elastic-plastic response of each layer. Partial loading-unloading curves were conducted using a cono-spherical tip (Figure 2B), with the unloading cycles at regular load increments used to derive the indentation stress-strain curves (Figure 2C) according to established protocols (Amini et al., 2015; Bertassoni and Swain, 2012). In such measurements, the contact stress corresponds to the mean contact pressure P_m (applied load divided by the contact area), and the strain is defined as the ratio of the radius of the contact area to the tip radius (Fisher-Cripps, 2011). In agreement with the single metrics E and H, the indentation yield stress (σ_y) derived from these curves was much larger in the outer layer than in the inner layer, both in dry (1.6 GPa versus 0.4 GPa) and even more prominently in hydrated conditions (1.4 GPa versus 0.045 GPa). The pronounced drop in σ_y of the inner layer is fully consistent with its high biopolymeric content (Amini and Miserez, 2013; Labonte et al., 2017) since water is well known to plasticize biopolymers.

Dynamic Micro-Mechanical Analysis

Viscoelastic materials, for example, materials containing a biopolymeric phase, are strongly affected by loading rates (Meyers and Chawla, 2009). Consequently, quasi-static characterization is not sufficient to assess their mechanical response, especially when considering the underlying function of the saddle structure as an elastic energy-storing device. To obtain a more quantitative picture of the dynamic mechanical response of the saddle, we used the nano-scale dynamic mechanical analysis capability of the nanoindenter and the "CMX" algorithm based on the Kelvin-Voigt model (Ferry, 1980), which allowed to obtain the storage (E') and loss (E'') moduli of the individual layers (Figure S1). In both dry and hydrated conditions, the outer layer exhibited higher moduli, in agreement with the static mechanical testing. Because of its *ca.* 10-fold higher storage modulus (Figure 2F), the outer layer is clearly capable of storing a higher amount of elastic energy compared with the inner layer (E' of 8.5 $\pm$ 1.5 versus 0.8 $\pm$ 0.5 GPa in hydrated conditions). This contrast in viscoelastic response between the two layers is perhaps even more apparent when considering the damping (dissipation) factor shown in Figure 2E ($\tan\delta = E''/E'$), which was 7- to 8-fold higher for the inner layer in both dry and hydrated states. These results demonstrate that whereas the inner layer exhibits significant dissipation of elastic energy ($\tan\delta = 0.51 \pm 0.03$ in the hydrated state), the outer layer has very low viscous loss ($\tan\delta = 0.06 \pm 0.01$ in the hydrated state), thus further confirming its role in storing elastic energy with minimum dissipative loss.

Tensile Properties of the Inner Layer: the Role of Chitin and Elastic Proteins

Because the inner layer of the saddle is subjected to tensile stresses, the moduli and yield strength values obtained by Hertzian nano-contact studies—whose measurements are in compressive loading—are not entirely representative of the loading regime that they are subjected to. On the other hand, it was not possible to mechanically exfoliate the inner layer from the outer layer without damaging the samples. Consequently, we probed the tensile response of the organic phase alone by conducting tensile testing on millimeter-scale, demineralized strips carefully extracted from the whole saddle, as illustrated in Figure 3A (top left inset). We were further interested in assessing the role of each phase in the tensile response. Therefore, one batch of samples was measured after a de-mineralization treatment in which only the mineral phase was removed, whereas the biopolymeric phases (chitin and protein) were retained. Subsequently, another batch of measurements was conducted after a second de-proteinization treatment, allowing to quantitatively differentiate the role of chitin and proteins on the tensile response. For both treatments, we previously verified that only the targeted phase was removed (Tadayon et al., 2015). Stress-strain curves of representative coupons from each batch are plotted in Figure 3A and show that the chitin/protein strips displayed a three-stage "*J*-shaped" tensile regime until failure, characteristic of many biopolymers and exemplified in collagen (Fratzl et al., 1998). The first region is the "toe" regime, which remained limited for the chitin/protein samples (ending at 2 pct strain). In this regime the stress-strain curve is non-linear, and we attribute this behavior to the partial alignment and straightening of the helicoidal chitin/protein fibrils, although *in situ* observations with synchrotron X-ray

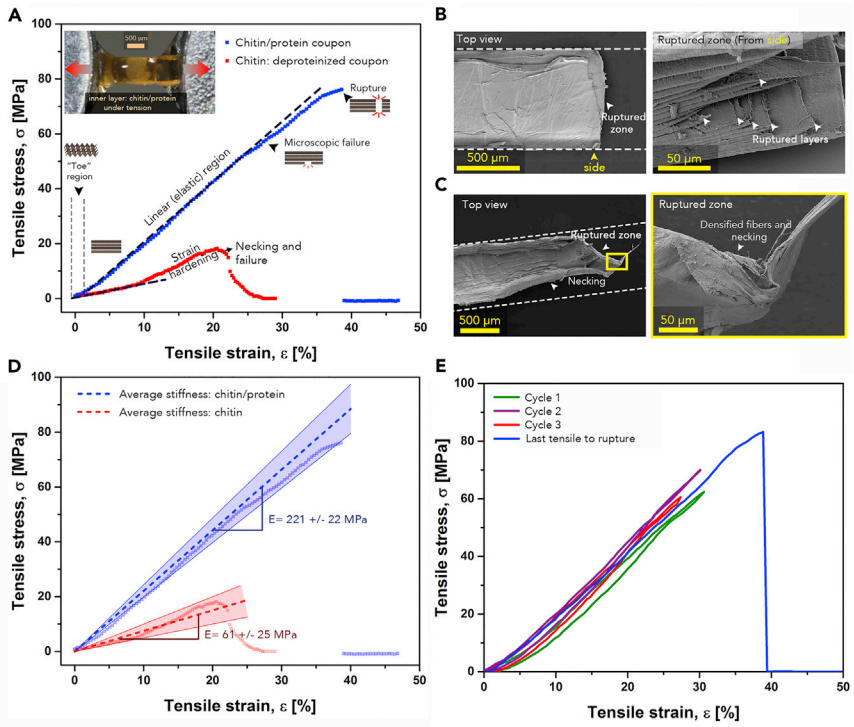

Figure 3. Tensile Properties of the Saddle Organic Phase

(A) Representative tensile stress-strain curves of de-mineralized (chitin/protein, blue) and de-mineralized and de-proteinized (chitin only, red) coupons in hydrated conditions. Protein/chitin coupons exhibit linear elastic deformation up to *ca.* 40 pct before rupture, whereas the chitin-only coupons display early plastic deformations as well as necking before rupture. The inset shows a de-mineralized sample fixed at its extremities before a tensile test.

(B) SEM micrographs of a ruptured chitin/protein coupon after tensile testing. Top view (left panel) and side view (yellow arrowhead in the left panel) show the layers' rupture (white arrowheads in the right panel).

(C) SEM micrographs of a ruptured chitin-only coupon. The left panel is a low-magnification micrograph, whereas the right panel represents a higher magnification of the ruptured zone. The dashed lines represent the width of each coupon before tensile testing.

(D) Fitted curves in the linear portion of tensile stress-strain curves for both types of samples. The dashed lines represent the mean values of the slopes in the linear regions (n = 7 and 8 for chitin/protein and chitin, respectively) and the shadow depicts the SDs.

(E) Cyclic tensile test performed on a chitin/protein strip showing the reversible response in the linear region up to 30 pct strain.

techniques would provide definitive experimental evidence (Holzapfel, 2008). Once the fibrils aligned with the loading axis, the second linear elastic regime was observed, which persisted until microscopic damage events at *ca.* 30 pct strain. In the final regime, elastic rupture occurred (at *ca.* 40 pct strain), with limited yielding or plastic deformation before macroscopic failure. We conducted these measurements while concomitantly observing the tensile coupons with a stereo-microscope. The mean rupture stress was σ_r = 75.1 $\pm$ 7.0 MPa and the strain to failure was ε = 34.5 $\pm$ 2.4 pct (n = 8) (Figure S2A). Cycling loading tests were also conducted (Figure 3E) and confirmed the fully elastic behavior (Figure S2B), as evidenced by the lack of irreversible deformation upon complete unloading and insignificant hysteresis.

For de-proteinized samples (red curve), a very distinctive behavior was observed when compared with the chitin/protein samples. These samples exhibited a lower elastic modulus as evidenced from the slope of the stress-strain curve in the elastic regime as well as deviation from the initial linear behavior at lower stress (σ_y = 4.2 $\pm$ 2.3 MPa; ε = 8.6 $\pm$ 2.0 pct, n = 7, Figure S2A) followed by strain hardening. Tensile coupons were simultaneously recorded during the experiments, and snapshots are shown in Figure S2C. These observations revealed necking in the gauge length, which started at σ = 15.2 $\pm$ 5.5 MPa and ε = 16.8 $\pm$ 4.0 pct, as deduced by the reduction in macroscopic cross-sectional area (Figure S2B).

SEM micrographs of ruptured samples are shown in Figures 3B and 3C. For the chitin/protein sample (Figure 3B, left panel), the width of the ruptured strip was still uniform and identical to the width of the sample before tensile testing (see the parallel dash lines) up to the rupture point, implying very little plastic deformation or necking and confirming an elastic type of deformation until failure. The right panel of Figure 3B shows a closer look at the fracture surface of the sample, showing individual layers that are all perpendicular to the tensile direction, suggesting no rearrangement of the layers until rupture. For the chitin-only coupon, on the other hand, SEM imaging confirmed necking and densification phenomena in the ruptured zone, as seen in the top and side views displayed in Figure 3C.

Since the inner layer is loaded in tension during saddle bending, one aim of the micro-tensile experiments was to gain insights into the tensile Young's modulus of the organic phase. From the slope of the linear part of stress-strain curves, we obtained $E = 221 \pm 22$ MPa for the chitin/protein and $E = 61 \pm 25$ MPa for chitin-only strips. Comparing these values with those obtained from sharp geometry nanoindentation on intact samples ($E = 900 \pm 160$ MPa) clearly indicates that the mineral phase, although less abundant than in the outer layer, still significantly contributes to the mechanical properties of the inner layer. Therefore, in subsequent FEM, we decided to use the elastic modulus of the inner layer measured by nanoindentation ($E = 900$ MPa). Although we recognize that the *tensile* modulus of the intact inner layer—containing both organic and mineral phases—may deviate from this value, the error associated with removing the mineral phase is deemed more substantial. Control simulations were, nevertheless, also carried out with an elastic modulus of 220 MPa inferred from the tensile tests on de-mineralized samples, and we found that this choice of elastic modulus did not significantly influence the overall internal stress distribution within the saddle.

Proteins Are Layer Specific

Flaws may be introduced on the edges of the tensile coupons during cutting the strips introduced, resulting in localized stress concentration that may result in premature failure. Despite this possible drawback, the chitin/protein strips exhibited significant reversible extensibility of *ca.* 30 pct, especially when compared with the coupons that were further de-proteinized. This clearly suggests that saddle proteins play a key role providing structural stability and elasticity to the inner layer. To gain further insights into the elastic proteins within each layer, we conducted quantitative amino acid analysis (Figure S3). The results revealed highly distinct amino acid composition between the inner and outer layers. Proteins from the inner layer were abundant in hydrophobic residues such as alanine (Ala, 17.2 mol. pct), glycine (Gly, 11.4 mol. pct), valine (Val, 11.1 mol. pct), and proline (Pro, 10.4 mol. pct), an amino acid composition that is reminiscent of elastic proteins such as elastin (Tatham and Shewry, 2002). This composition strongly differed with that of the outer layer, which was much richer in acidic residues such as aspartic acid (Asp) and glutamic acid (Glu) that accounted for 8.3 and 9.2 mol. pct, respectively. Given that proteins that control biomineralization of calcified tissues are well known to be enriched with acidic residues (Falini et al., 1996; Belcher et al., 1996), such a biased amino acid composition is to be expected. Overall, the amino acid composition results indicate that distinct sets of proteins are present in each layer, although their identity and primary structure remain unknown at the moment.

Flexural Stiffness of Miniature Cantilevers

To experimentally validate the hypothesis that the spatial phase distribution in the saddle leads to optimum storage of elastic energy, we conducted micro-bending experiments on miniature-cut cantilevers extracted from a saddle using a picosecond-laser cutting technique (Figure S4). The SEM micrograph in the inset of Figure 4A shows such a miniature cantilever, color-shaded as yellow and green for the outer and the inner layers, respectively. The miniature cantilevers were loaded in bending with a custom-made stainless steel spherical tip (350 μm radius) using the high-load transducer (maximum load of 10 N) of our nanoindenter equipment. Two types of loading configurations were applied to the miniature cantilevers (Figure 4A). In the first one, the loading point during bending was applied to the inner layer. This configuration is referred as "normal" since it corresponds to the loading regime in the saddle during a native strike, namely, the outer layer is in compression and the inner layer in tension. The second configuration had an opposite geometry, with the loading point applied to the outer layer such that the latter was subjected to tensile stresses, whereas the inner layer was under compression. This configuration is hereafter referred to as "reverse." In each case, identical experimental conditions were imposed, i.e., bending distance (distance from the loading point to the fixed point) of 900 μm and maximum deflection of 60 μm.

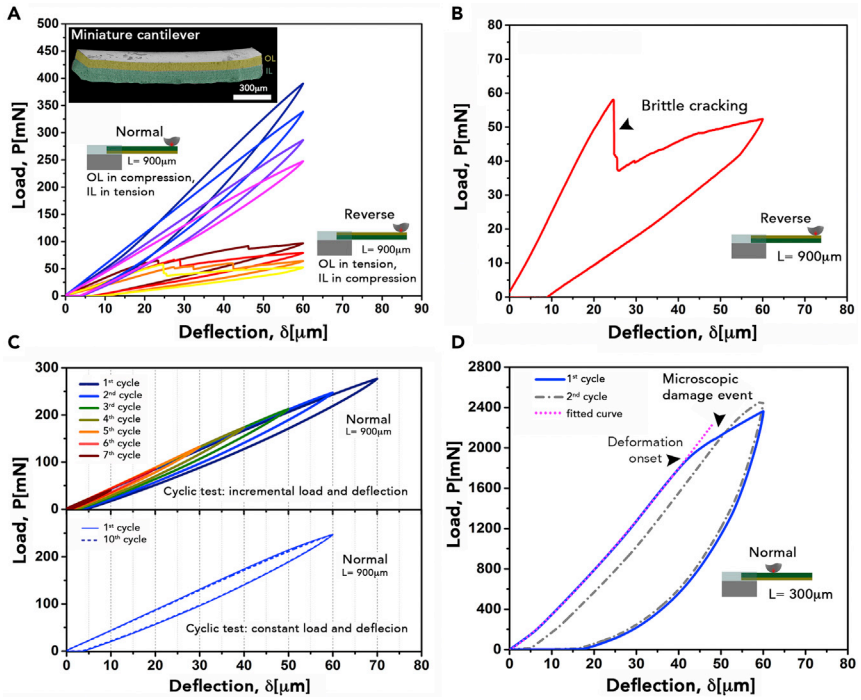

Figure 4. Micro-Bending Experiments on Miniature Cantilevers Cut from a Saddle by Picosecond Laser Machining

(A) Loading-deflection curves of 8 cantilevers (4 in the "normal" configuration and 4 in the "reverse" configuration) subjected to bending moment (distance from the contact point to the fixed point, L = 900 μm). Miniature cantilevers in "normal" configuration exhibit a higher flexural rigidity and maximum bending strength compared with the "reverse" configuration.

(B) Zoom-in of a load-deflection curve in the "reverse" configuration, highlighting load discontinuity associated with brittle macro-damage.

(C) Cyclic micro-bending experiments in the "normal" configuration with increasing (top) or constant (bottom, 10 cycles) peak loads between consecutive loading cycles. Note that the 10th cycle in the bottom panel follows the identical trace as the first cycle, denoting no damage and fully elastic deformation (the residual deflection is attributed to sliding of the tip at its contact point and not to irreversible deformation of the cantilever).

(D) Load-deflection curve in the "normal" configuration with a lower bending distance of 300 μm. No brittle damage events were detected, but the slope change during loading denotes plastic deformation, as also confirmed by the 15-μm irreversible deflection upon unloading.

Representative results from these micro-bending experiments are shown in Figures 4A–4C. In the "normal" configuration, the load-deflection curves displayed an elastic deformation response with a continuous increase of load up to the maximum deflection and a relatively high flexural stiffness. The flexural response of the miniature cantilevers in the "reverse" configuration markedly differed. These samples exhibited a much lower flexural stiffness as well as discontinuities in the load-deflection curves that were detected at loads as low as 50 mN, which can be attributed to micro-failure events due to brittle cracking in the outer layer. An enlarged view of such an event is shown in Figure 4B, and this type of behavior was consistently detected for all miniature cantilevers in the "reverse" configuration. Confirmation that the discontinuity was linked to micro-damage was further evidenced by the strong decrease in the slope of the load-deflection curve immediately following the load drop, indicating a reduced load-bearing ability. In contrast, no damage could be detected in the "normal" configuration, including in cycling testing (Figure 4C), for which the peak load between consecutive cycles was either incrementally increased (top) or kept constant (bottom). For example, in the latter experiment, the loading/unloading paths were identical in consecutive cycles, suggesting elastic loading with no internal damage. Furthermore, miniature cantilevers in the normal configuration were very robust in these bending experiments and no damage could be detected within the displacement limit of our equipment (80 μm maximum z displacement). Failure could only be initiated by reducing the bending distance to 300 μm so as to increase the bending moment and stresses in the miniature cantilevers, as shown in Figure 4D where damage initiated at load as high as 1800 mN.

	"Normally" Loaded Cantilevers [4]	"Reversely"-Loaded Cantilevers [5]
Flexural modulus, E_b (GPa)	9.8 ± 1.8	4.9 ± 0.7
	$p < 0.05$	
Work-of-fracture, W (J·m^{-2})	647.9 ± 86.4	7.8 ± 0.6
	$p < 0.01$	
Maximum stress[a] (MPa)		
Outer layer, $\sigma_{max,\ OL}$	−433.9 ± 93.3	41.7 ± 2.9[a]
Inner layer, $\sigma_{max,\ IL}$	114.7 ± 25.6[a]	−10.3 ± 0.6

Table 1. Calculated Mean Flexural Moduli and Work-of-Fracture of Miniature Cantilever in the "Normal" and "Reverse" Loading Configurations

Numbers in brackets represent the number of cantilevers tested.

[a]Internal stress at which failure occurred.

Next, we calculated the flexural modulus and nominal work-of-fracture for each loading configuration. The flexural modulus, E_b (GPa), was obtained from the slope of the load-deflection curve in the elastic region and the nominal work-of-fracture, W (J·m^{-2}), was extracted from the area under the load-deflection curves normalized by the cross-sectional area, according to the following equations:

$$W = \frac{\int_0^{\delta_f} P d\delta}{ab} \quad \text{(Equation 1)}$$

$$E_b = \frac{PL^3}{3I\delta} \quad \text{(Equation 2)}$$

$$I = \frac{ab^3}{12} \quad \text{(Equation 3)}$$

where P is the load (N), L the span of the bending test (m), I the moment of inertia (m^4), a the specimen width (m), b the specimen height (m), and δ the deflection (m). The results are shown in Table 1. Notably, the mean work-of-fracture in the normal configuration (~ 648 J·m^{-2}) was nearly two orders of magnitude higher than in the reverse configuration (~7.8 J·m^{-2}), thus demonstrating that the saddle design allows to maximize the amount of stored elastic energy.

Considering the bilayer structure of the cantilever beams, and knowing the thickness and elastic modulus of each layer, a quantitative evaluation of the maximum stress levels in the layers can be obtained. The outer and inner layer thickness of each cantilever was measured by optical microscopy, while the elastic modulus of each layer were input from the results of micro-mechanics experiments. For the outer and inner layer, we have E_{OL} = 10 GPa and E_{IL} = 900 MPa, respectively, the justification for which was previously described. For a bilayer miniature cantilever, the maximum stress in each layer is located on the surface and given by (Timoshenko and Goodier, 2001):

$$\sigma_{max,OL} = \frac{-M\delta E_{OL}}{E_{OL}I_{OL} + E_{IL}I_{IL}} \quad \text{(Equation 4)}$$

$$\sigma_{max,IL} = \frac{-M\delta E_{IL}}{E_{OL}I_{OL} + E_{IL}I_{IL}} \quad \text{(Equation 5)}$$

where M is the bending moment (N·m^{-1}) and I_{OL} and I_{IL} are the moments of inertia of the individual layers (outer and inner layer, respectively). For the "normal" configuration, these calculations reveal that the maximum stresses at the onset of failure (refer to Figure 4D) were −433.8 ± 93.3 MPa (compression) and 114.7 ± 25.6 MPa (tension) for the outer and the inner layers, respectively. We note that the maximum compressive stress in the outer layer falls below the yield strength obtained by contact mechanics measurements (1.4 GPa), although it must be noted that the contact stress beneath the spherical tip is not purely compressive and thus not directly comparable. Nevertheless, the maximum compressive stress at the onset of failure appears to be small enough to remain in the elastic range. On the other hand, the maximum tensile stress in the inner layer exceeds the yield strength and failure stress measured by indentation and tensile measurements, respectively, suggesting that failure was initiated in the inner layer.

The yield stress previously obtained by Hertzian nano-contact mechanics (Figure 2) are derived mostly from a compressive stress field, whereas the values measured by tensile measurements were conducted on samples that were de-mineralized. From this perspective, the failure stress in the inner layer (114.7 MPa) obtained from the miniature cantilever experiments are viewed as more accurate of the actual saddle behavior. In the "reverse configuration," the maximum (tensile) stress in the outer layer at failure was 41.7 $\pm$ 2.9 MPa and the maximum (compressive) stress in the inner layer was -10.3 ± 0.6 MPa. Compared with the "normal" loading configuration, these much lower stress values confirm that the inner layer is indeed much weaker under compressive stresses, as well as the intrinsic brittleness of the outer layer under the tensile stress regime imposed by the "reverse" configuration (Figure 4A). Overall, these simple calculations demonstrate that the normal loading configuration allows to generate much higher elastic stresses within the saddle before inducing micro-damage. Consequently, the saddle design results in the ability to store a relatively high density of elastic energy.

Stress Distribution in the Saddle during Loading by FEM

Owing to the complex macroscopic geometry of the saddle, we used FEM to quantify the stress distributions and monitor the deformation in the whole saddle structure during loading. A three-dimensional (3D) model of the saddle was generated from scanning electron micrographs and micro-computed tomography (CT) scans of a saddle by fitting 16 longitudinal and transversal cuts of the 3D scan with parabola equations. Due to symmetrical constraints of the hyperbolic-paraboloid saddle structure, a 3D model was then reconstructed from these fitted curves (Figures S5A–S5C). As input material properties for modeling, we used the values obtained from nanoindentation measurements. For the density ρ and the Poisson's ratio ν, we used the values from previous modeling of the mantis shrimp dactyl club (Amini et al., 2015).

Outer layer: E_{OL} = 10 GPa, ρ_{OL} = 2.5 g/cm^3; ν_{OL} = 0.25

Inner layer: E_{IL} = 0.9 GPa, ρ_{IL} = 1.5 g/cm^3; ν_{IL} = 0.30

The reconstructed 3D saddle in the resting mode is shown in Figure 5A (top panel). A 20 N force was then applied longitudinally (x direction) to the saddle, a value selected from our previous study and that corresponds to the external load at which damage was initiated in whole saddles (Figure S5D). During loading, the saddle flattened in agreement with our previous experimental measurements (Tadayon et al., 2015). The stress distribution in all principal directions as well as the von Mises stresses are presented in Figure S6, and the stress distribution of the third principal stress is displayed in Figure 5A (bottom panel). The maximum compressive stress in the outer layer corresponded to the third stress invariant and reached -128 MPa, whereas the maximum stress in the inner layer was the first principal stress and attained 50 MPa (Figure S6). We note that the maximum third principal stress in the outer layer (-128 MPa) was well below the yield stress measured by Hertzian contact studies (1.4–1.6 GPa) (Figure 2C), indicating that even at relatively high external loads (20 N), the stresses generated in the saddle remained within the elastic regime.

An interesting result from the FE modeling is that the neutral axis (zero internal stress) for all three principal stresses is located very close to the outer/inner layer interface. This design likely minimizes the risk of failure by interfacial delamination. Indeed, interfaces are typically weak spots of bilayer structures and interfacial delamination usually leads to irreversible structural damage (Akbarov, 2013). Since the saddle bilayer interface is subjected to minimal stresses, interfacial delamination is thus likely to be prevented, suggesting an additional optimization of the saddle geometry adapted to its function. To the best of our knowledge, this optimization of very low internal stress near the interface has previously not been reported in biological materials. Another notable finding from the simulations is that surface stresses are uniformly distributed. In other words, stress concentration points are avoided on the saddle surfaces.

FEM results provide further insight into the continuum design of the saddle. The magnitudes of the maximum compressive stress of the second and third stress invariants, which are two perpendicular components, were found to be almost equal on the saddle surface, i.e., 121 MPa and 128 MPa, respectively (Figure S6). Based on the principal stresses vector contour on the outer surface and in proximity to the saddle point, the third principal stress is aligned in the x direction and the second principal stress vector in the z direction (Figure S7). Therefore, the resultant component is inclined at almost 45° in the xz plane of the outer surface, consistent with the shear-induced diagonal crack pattern observed on the

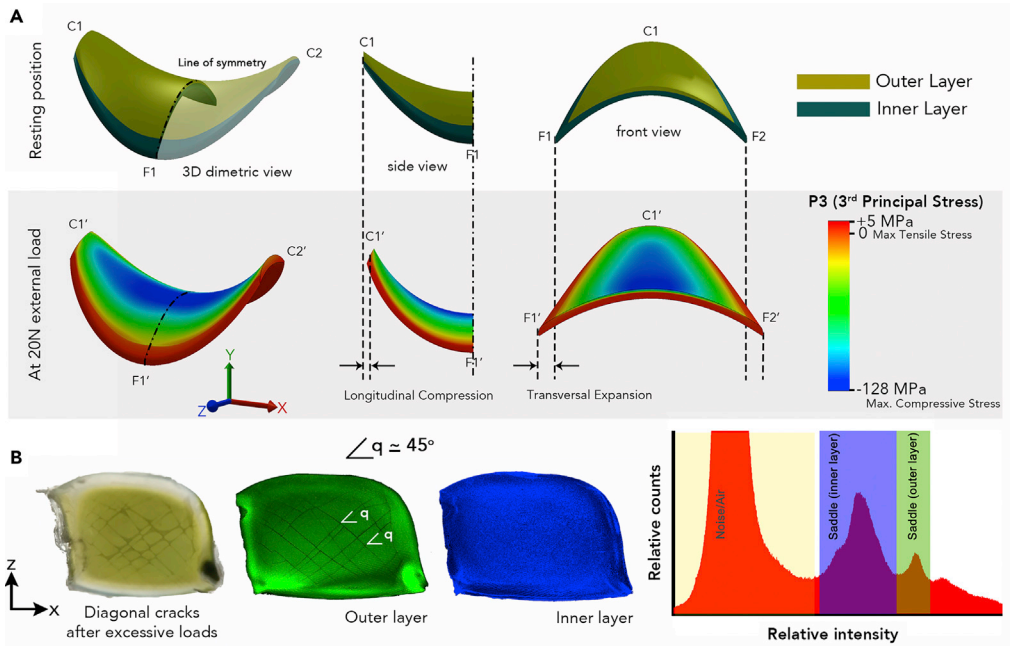

Figure 5. Stress Distributions in the Saddle during Loading as Modeled by 3D FEM and Crack Pattern after Loading Until Surface Damage was Observed

(A) FEM of the 3D saddle under compressive longitudinal loading. The top panel corresponds to the reconstructed half saddle geometry in the resting condition from dimetric, side, and front views. The reconstructed structure is represented with its two main layers: the outer layer in dark yellow and the inner layer in green. The bottom panel represents the third principal stress distribution in the deformed saddle under an external longitudinal load of 20 N.

(B) Macro-photos of fracture patterns of a saddle loaded until failure illustrating the presence of surface diagonal cracks oriented at *ca.* 45° with respect to the loading axis. The two microCT images of the saddle (middle images) were filtered by the density of the outer (green) and the inner (blue) layers, respectively. These images demonstrate that when the saddle was loaded until macroscopic cracks were visible, all cracks nucleated in the outer layer, whereas the inner layer remained uniform and no failure was detected.

surface when the saddle was compressed until failure (Tadayon et al., 2015). Figure 5B presents X-ray tomography results for the saddle with a "tiling" cracking pattern on the outer surface consisting of two series of elongated cracks, running across nearly the entire surface and at *ca.* 45° from the loading axis (x direction). Despite the formation of surface cracks, the saddle was found to be able to sustain significant load beyond surface cracking formation with no catastrophic failure. The 45° angle between the crack direction and the applied loading axis further corroborates that cracks were nucleated along shear bands (Timoshenko and Goodier, 2001) which is consistent with a uniform stress distribution since most cracks appeared almost concomitantly during the experiments. We can also compare the elastic energy stored in the saddle as computed by FEM (the area under the load-displacement curve) with the average value previously obtained experimentally (Tadayon et al., 2015). At the applied load of 20 N, the experimental stored energy was 1.4 mJ, whereas the FEM calculated values for the dry and fully hydrated saddles were 0.7 mJ and 5.3 mJ, respectively (Figure S8), indicating that the experimental stored energy is between the calculated values for the hydrated and the dry conditions, but closer to the dry saddle. We attribute this result to two main reasons. First, the elastic modulus in hydrated conditions was obtained by nanoindentation measurements on cross sections of the saddle, where the sample surface was fully immersed and water could freely ingress within the material during testing. However, in the intact saddle, water cannot fully penetrate in the inner layer because of the outer wax coating that prevents water adsorption in the bulk. In addition, during compressive tests of whole saddles, we initially hydrated the saddle, but our device did not allow us to conduct the test in fully immersed conditions. Because of these combined effects, it is likely that the saddles were partially hydrated during compressive testing (which may represent the native conditions because the waxy coating may prevent water adsorption in the bulk), with a load-displacement response bound by hydrated and dry conditions but closer to the latter.

Further analysis of the microCT scans filtered for the inner layer density (Figure 5B, blue) revealed that even when the applied load was large enough to nucleate surface cracks in the outer layer, no sign of internal macroscopic failure was detected in the inner layer (Figure 5B, green), although our cantilever bending test (Figure 4D) suggests that micro-scale damage may exist. Finally, the simulations confirmed the much higher elastic stresses generated in the outer layer compared with the inner layer, firmly establishing the role of the outer layer in storing the elastic energy during saddle loading.

DISCUSSION

This study reveals a refined picture of the mechanical design of the mantis shrimp saddle, a bilayer complex spring and the stiffest element in the power amplification system used by the mantis shrimp to store elastic energy for its powerful strikes of the dactyl club. Quasi-static and dynamic contact mechanics measurements of individual layers have shown that the outer layer plays the key role of storing elastic energy: its high elastic modulus and yield strength ensure energy storage capability while preventing internal micro-damage during loading. The inner layer, on the other hand, is characterized by a high damping factor, and its main function is to sustain tensile stresses generated during compressive loading of the saddle. Were the saddle only made of the highly mineralized outer layer material, it would fail because of the intrinsic weakness of mineralized phases when subjected to tensile stresses. Micro-bending experiments experimentally corroborate these findings. Miniature cantilevers loaded in a configuration corresponding to the native conditions are able to sustain higher external loads and can store up to two orders of magnitude more elastic energy before failure than in the reverse loading configuration.

FEM of the saddle under external compressive forces predicted that the maximum principal stress in the outer layer remains well below the yield stress. Given the relative brittleness of the outer mineralized layer, such a high "safety factor" ensures that this layer is loaded well within the elastic regime, thereby preventing fatigue-induced micro-cracking that would be extremely harmful for the saddle function. Additional observations on the failure process of the whole saddle revealed that failure occurs by crack nucleation and propagation on the surface of the outer layer and is mainly due to the flattening effect in the saddle under compression, whereas no observable defect occurs in the inner layer. Uniform cracking pattern on the outer layer surface is in agreement with the uniform stress distribution predicted from FEM.

Our findings imply that the mantis shrimp saddle-like spring has been optimized at the geometrical, and meso- and micro-structural levels. Macroscopically, the saddle geometrically ensures uniform loading, preventing stress concentration. Meso-scale phase distribution leads to storage of elastic energy by compressive loading of the biomineral-rich outer layer with minimal viscoelastic loss, whereas the inner layer provides tensile support to the saddle during bending. Finally, the neutral axis is located near the outer/inner layer interface, thereby shielding the saddle from deleterious interfacial delamination.

The study also offers useful lessons to improve elastic energy storage devices in various applications, notably in micro-robotics. More efficient devices could be engineered using stiff and light materials such as ceramics since this would enhance the strain energy density that can be stored. In practice, such design is usually avoided due to the intrinsic brittleness of ceramics building blocks. The saddle structure provides a bioinspired design to overcome this limitation. To successfully mimic the complex saddle spring, additive manufacturing with judicious selection of materials for the bilayer components is deemed the method of choice.

Limitations of the Study

In tensile studies of the inner layer, owing to the complex shape of the saddle and technical challenges in extracting the original inner layer in strips, we used demineralized samples. As a result, the exact tensile response of the chitin/protein/mineral composite of the inner layer is not fully known, and these data would be more reliable input for FEM. The second constraint of the FEM studies is that we used an ideal hyperbolic-paraboloid structure as a simplified model of the native saddle; however, the latter is not fully symmetrical. Furthermore, FEM yield a good estimation of the elastic energy stored before striking, but not of the released energy, which happens much faster. For such computations, the viscoelastic properties of the material (especially the inner layer) would need to be taken into account. And finally, although the saddle is considered the main component of the power amplification system storing the elastic energy in the dactyl club, there are other components, such as the meral-V (Patek et al., 2007), which may also have a significant biomechanical contribution.

METHODS

All methods can be found in the accompanying Transparent Methods supplemental file.

SUPPLEMENTAL INFORMATION

Supplemental Information includes Transparent Methods and ten figures and can be found with this article online at https://doi.org/10.1016/j.isci.2018.08.022.

A video abstract is available at https://doi.org/10.1016/j.isci.2018.08.022#mmc2.

ACKNOWLEDGMENTS

We thank Dr. Hajar Razi and Dr. Lorenzo Guiducci for advice on FEM. This research was funded by the Singapore National Research Foundation (NRF) through an NRF Fellowship awarded to A.M. M.T. and S.A. were supported by a Singapore International Graduate Award (SINGA fellowship).

AUTHOR CONTRIBUTIONS

M.T. conducted all experiments and FEM and performed all data analysis. S.A. helped conduct nanoindentation experiments and FEM. Z.W. helped in ps-laser cutting of the miniature cantilevers. A.M. supervised the study. M.T. and A.M. wrote the paper with input from all authors.

DECLARATION OF INTERESTS

The authors declare no competing interests.

Received: May 6, 2018
Revised: August 2, 2018
Accepted: August 27, 2018
Published: October 18, 2018

REFERENCES

Akbarov, S. (2013). Buckling delamination of elastic and viscoelastic composite plates with cracks. In Stability Loss and Buckling Delamination (Springer), pp. 135–267.

Amini, S., and Miserez, A. (2013). Wear and abrasion resistance selection maps of biological materials. Acta Biomater. *9*, 7895–7907.

Amini, S., Tadayon, M., Idapalapati, S., and Miserez, A. (2015). The role of quasi-plasticity in the extreme contact damage tolerance of the stomatopod dactyl club. Nat. Mater. *14*, 943–950.

Belcher, A.M., Wu, X.H., Christensen, R.J., Hansma, P.K., and Morse, D.E. (1996). Control of crystal phase switching and orientation by soluble mollusc-shell proteins. Nature *281*, 56–58.

Bertassoni, L., and Swain, M. (2012). Influence of hydration on nanoindentation induced energy expenditure of dentin. J. Biomech. *45*, 1679–1683.

deVries, M., Murphy, E., and Patek, S. (2012). Strike mechanics of an ambush predator: the spearing mantis shrimp. J. Exp. Biol. *215*, 4374–4384.

Erickson, G.M., Gignac, P.M., Lappin, A.K., Vliet, K.A., Brueggen, J.D., and Webb, G.J.W. (2014). A comparative analysis of ontogenetic bite-force scaling among Crocodylia. J. Zool. *292*, 48–55.

Falini, G., Albeck, S., Weiner, S., and Addadi, L. (1996). Control of aragonite or calcite polymorphism by mollusk shell macromolecules. Science *271*, 67–69.

Ferry, J.D. (1980). Viscoelastic Properties of Polymers (Wiley).

Fisher-Cripps, A.C. (2011). Nanoindentation (Springer Science+Business Media, LLC).

Forterre, Y., Skotheim, J.M., Dumais, J., and Mahadevan, L. (2005). How the Venus flytrap snaps. Nature *433*, 421–425.

Fratzl, P., Misof, K., Zizak, I., Rapp, G., Amenitsch, H., and Bernstorff, S. (1998). Fibrillar structure and mechanical properties of collagen. J. Struct. Biol. *122*, 119–122.

Holzapfel, G. (2008). Collagen in arterial walls: biomechanical aspects. In Collagen, P. Fratzl, ed. (Springer), pp. 285–324.

Labonte, D., Lenz, A.-K.K., and Oyen, M.L. (2017). On the relationship between indentation hardness and modulus, and the damage resistance of biological materials. Acta Biomater. *57*, 373–383.

Lawn, B. (1993). Fracture of Brittle Solids (Cambridge University Press).

Meyers, M.A., and Chawla, K.K. (2009). Mechanical Behavior of Materials (Cambridge University Press).

Meyers, M.A., Lin, A.Y.M., Seki, Y., Chen, P.Y., Kad, B.K., and Bodde, S. (2006). Structural biological composites: an overview. JOM *58*, 35–41.

Patek, S., and Caldwell, R. (2005). Extreme impact and cavitation forces of a biological hammer: strike forces of the peacock mantis shrimp *Odontodactylus scyllarus*. J. Exp. Biol. *208*, 3655–3664.

Patek, S.N., Baio, J.E., Fisher, B.L., and Suarez, A.V. (2006). Multifunctionality and mechanical origins: ballistic jaw propulsion in trap-jaw ants. Proc. Natl. Acad. Sci. USA *103*, 12787–12792.

Patek, S.N., Korff, W.L., and Caldwell, R.L. (2004). Biomechanics: deadly strike mechanism of a mantis shrimp. Nature *428*, 819–820.

Patek, S.N., Nowroozi, B.N., Baio, J.E., Caldwell, R.L., and Summers, A.P. (2007). Linkage mechanics and power amplification of the mantis shrimp's strike. J. Exp. Biol. *210*, 3677–3688.

Ritchie, R.O. (2011). The conflicts between strength and toughness. Nat. Mater. *10*, 817–822.

Tadayon, M., Amini, S., Masic, A., and Miserez, A. (2015). The mantis shrimp saddle: a biological spring combining stiffness and flexibility. Adv. Funct. Mater. *25*, 6437–6447.

Tatham, A.S., and Shewry, P.R. (2002). Comparative structures and properties of elastic proteins. Philos. Trans. R. Soc. Lond. B Biol. Sci. *357*, 229–234.

Timoshenko, S.P., and Goodier, J.N. (2001). Theory of Elasticity (McGraw-Hill).

ISCI, Volume *8*

Supplemental Information

Biomechanical Design of the Mantis Shrimp Saddle: A Biomineralized Spring Used for Rapid Raptorial Strikes

Maryam Tadayon, Shahrouz Amini, Zhongke Wang, and Ali Miserez

Supplemental Information

Figures

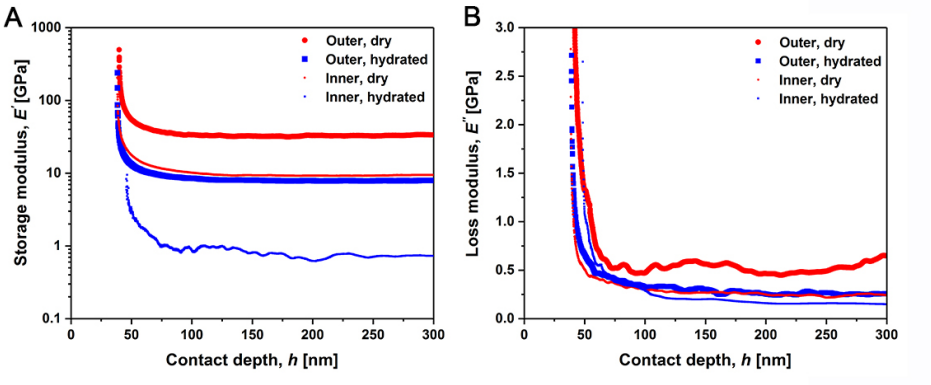

Figure S1. CMX (Continuous Measurement of X) depth profile as a function of contact depths in the range 50 to 300 nm for the two different layers of the saddle (related to Figure 2). The storage (**A**) and loss moduli (**B**) of the saddle outer and the inner layers show a decrease in both moduli from dry to hydrated conditions. In both hydrated and dry conditions, the storage modulus of the outer layer is higher.

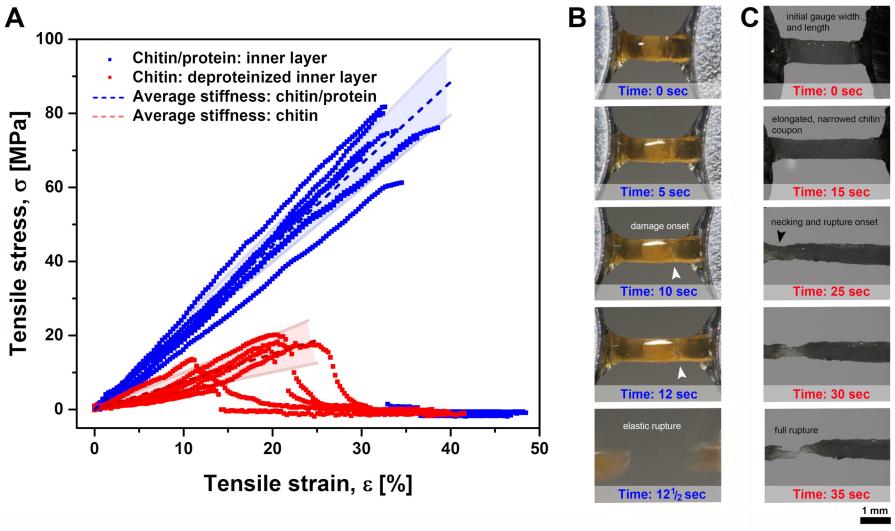

Figure S2. Tensile test on demineralized coupons (related to Figure 3). (**A**) Tensile stress-strain curves of all tested samples in this study. Chitin/protein in blue, and chitin only in red. Time-lapse of (**B**) chitin/protein samples and (**C**) chitin only samples during tensile testing, which were concomitantly video-recorded during the experiments.

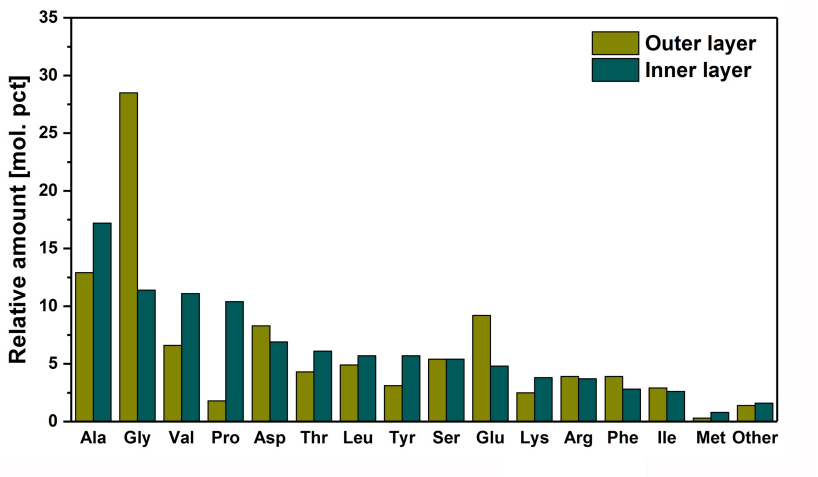

Figure S3. Layer-specific amino acid composition (related to Figure 3). The relative amount of each amino acid in each layer was obtained by Ninhydrin-based amino acid analysis. Note the enrichment of acidic residues (glutamic acid and aspartic acid) in the outer, heavily mineralized layer, and proline and valine in the inner, bio-polymeric layer.

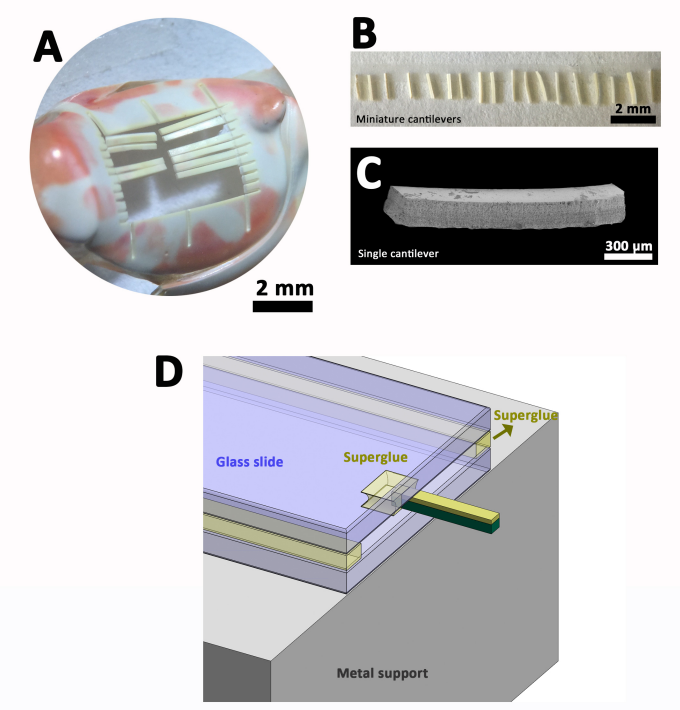

Figure S4. Miniature cantilevers and their fixation for micro-bending testing (related to Figure 4). (**A**) Picosecond-laser cut cantilevers from the saddle. (**B**) All cantilevers detached from the saddle after ps-laser cuttting. (**C**) SEM micrograph of a single cantilever. (**D**) The cantilever holder including the top and bottom glass slides, a metal support and superglue to fix the edge of the cantilevers. The schematic illustrates that the superglue is in contact with the base of the cantilever half-way within the glass slides holders, *i.e.* there was no superglue at the edge of the cantilever to avoid contamination in the sample gauge length.

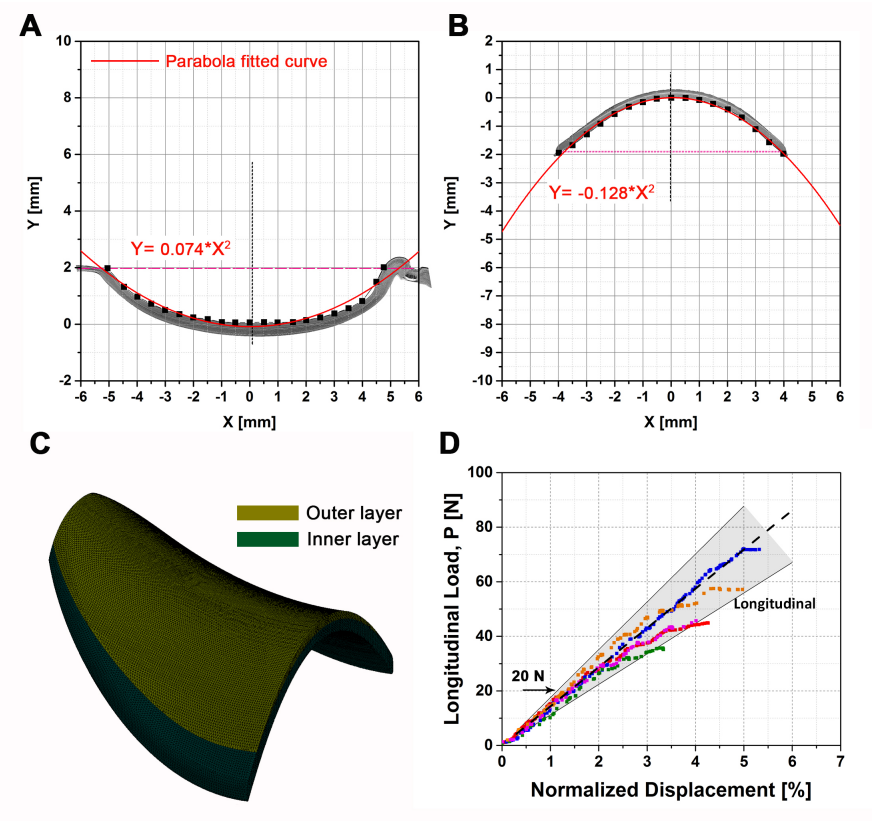

Figure S5. Saddle geometrical features and inputs for 3D construction and FE analysis (related to Figure 5). Parabola formula used to fit the (**A**) longitudinal and (**B**) transversal cross-section of the saddle at the saddle point. (**C**) Reconstructed saddle as a double ruled surface shape, and meshed symmetrical model with the two distinct layers. (**D**) Load-displacement curves of the saddle under macroscopic compression testing from a previous study (TADAYON et al., 2015), used to choose the relevant external load values as input for FE computations.

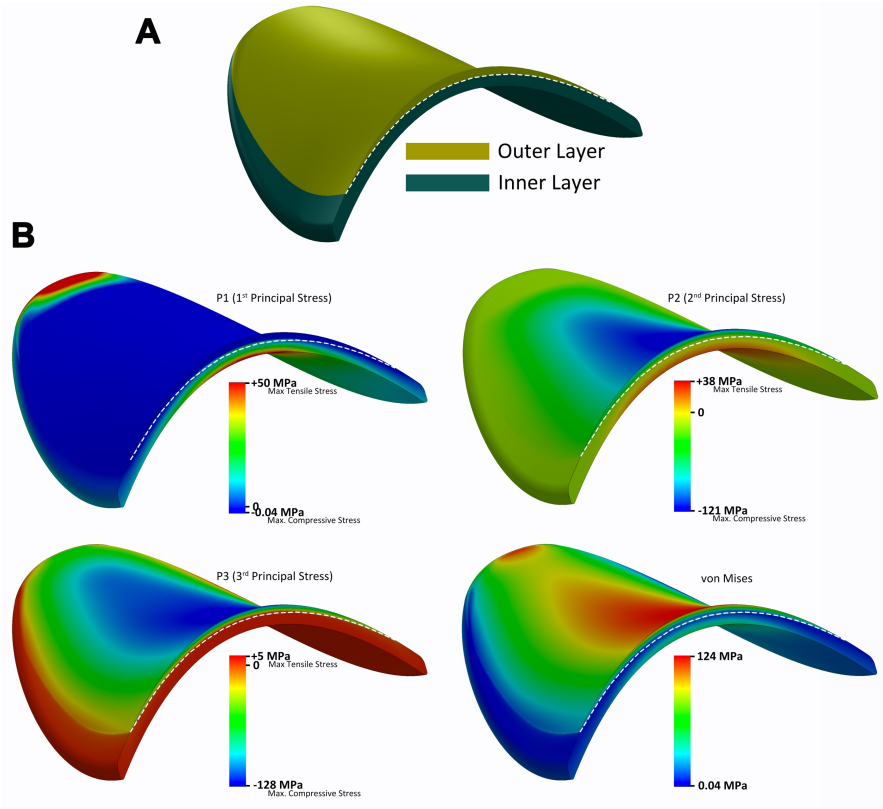

Figure S6. Principal and von Mises stresses distribution in the saddle based on FEM (related to Figure 5). (**A**) Symmetrical reconstructed model before computations. (**B**) Principal stresses and von Mises stress distribution in the whole structure at the external peak load. The location and magnitude of the maximum tensile and compression stresses are shown. The dash line delineates the interface between the outer and the inner layer, showing that the interface is located where the principal stresses are close to zero or where the von Mises stress is minimum (lower right).

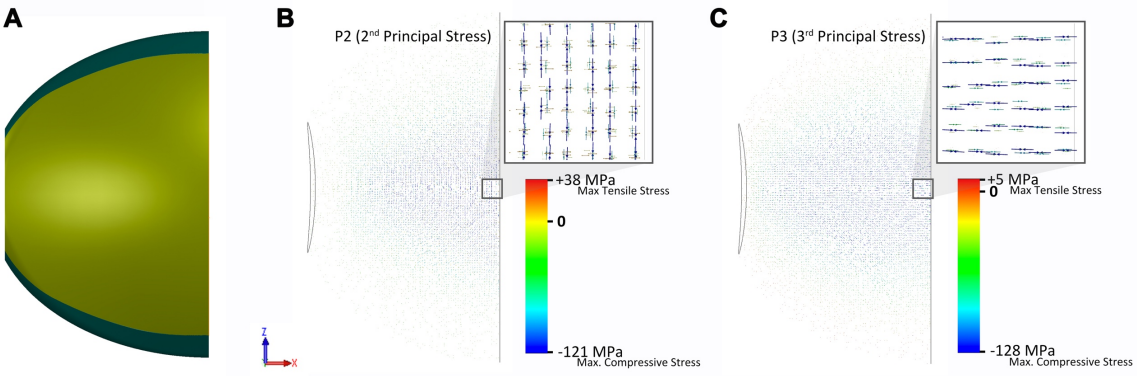

Figure S7. Principal stress vector plots obtained from FEM (related to Figure 5). (**A**) Reconstructed model of the saddle in the *xz*-plane view before computations. (**B**) 2nd principal stress vector plot in the *xz*-plane, indicating that the maximum principal (compressive) stresses on the surface (in blue) are oriented perpendicular to the loading direction (*z*-direction). The weaker tensile stress vectors in orange or red are the principal stress directions beneath the surface. (**C**) 3rd principal stress vector plot in the *xz*-plane plane, showing that the principal directions are oriented along the loading direction (*x*-direction).

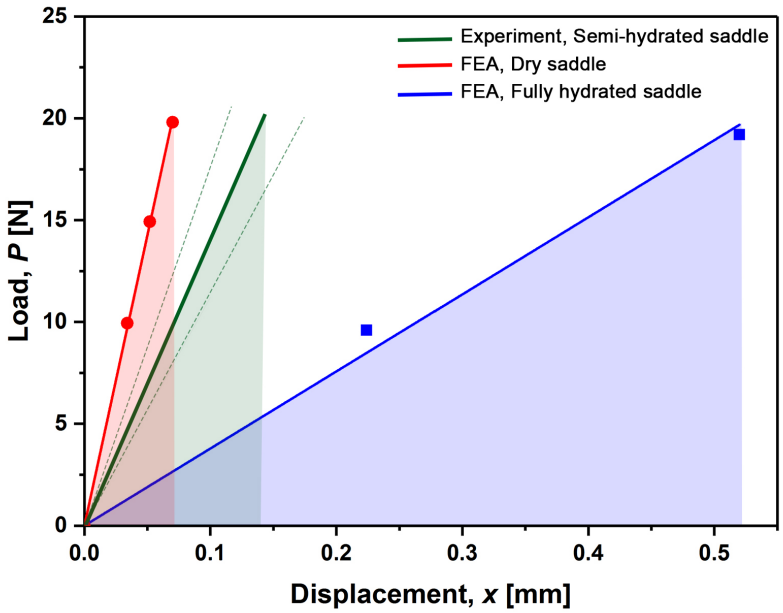

Figure S8. Load-displacement curves obtained from experiments and by FEM (related to Figure 5). The green dotted lines correspond to the range of experimental curves and the solid green curve is the average of all experimental curves. The area under each curve corresponds to the elastic potential energy stored in the saddle at 20 N of applied load.

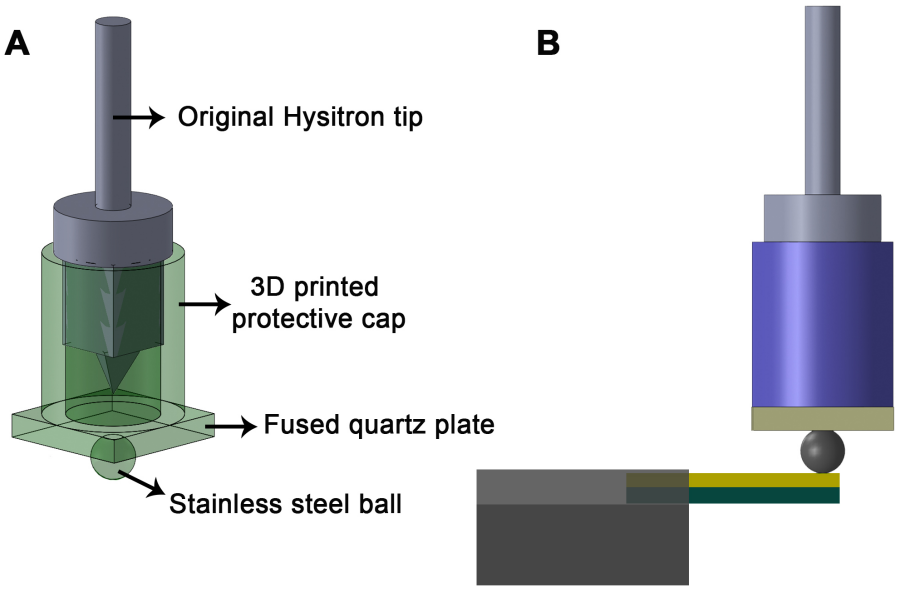

Figure S9. Customised indentation tip and bending test setup nano-mechanical experiments (related to Figure 4). (**A**) Customised 350 μm radius stainless steel spherical tip attached to the force transducer of the Hysitron Triboindenter. (**B**) Schematic of the bending test setup. Force and displacement were axially measured using the force/displacement of the nanoindenter equipment.

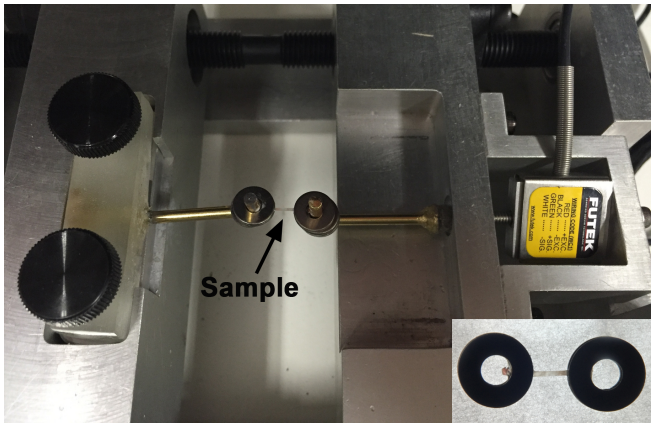

Figure S10. Custom-made micro uniaxial testing machine used to conduct tensile tests on the chitin/protein and chitin only coupons (related to Figure 3). A coupon fixed between the washers is shown in the inset.

Transparent Methods

Research Specimens (Saddle). Specimens of *Odontodactylus scyllarus* (Figure 1) and *Harpiosquilla harpax* representing the smasher and the spearer types of mantis shrimps, respectively, were obtained from local markets in Singapore. Their appendages were dissected and immediately stored at -20° C. For experiments in which the saddle had to be separated from the other parts of the appendage, the saddle was carefully dissected with a scalpel and later washed with deionized water to remove residual salt and organic debris. Samples were embedded in Epoxy cold mounting resin (EpoFix Kit, Struers), cut using a linear precision diamond saw IsoMet 4000 (Buehler, USA), and subsequently polished with P1200/4000 grade SiC paper. To obtain a well-polished and mirror-smooth surfaces, 1 μm diamond paste followed by 40 nm colloidal silica suspension were used during polishing. To remove silica particles and wash away debris, the polished samples were cleaned in an ultrasonic bath for 5 minutes in 5:1 volume ratio of a water:ethanol solution between each polishing step.

Microstructural Imaging and Characterization. Microscopical images of the tensile samples were obtained using a field emission scanning electron microscopope (FESEM),

JEOL 7600F. A platinium coating approximately 5-10 nm thick coating was deposited on the samples, which were imaged using a lower secondary electron imaging (LEI) detector at an accelerating voltage of 5 KV. Photographs of the mantis shrimp and their appendages were captured using an EOS 700D camera equipped with an EF 100 Macro lens (Canon, Japan). A Zeiss Stemi DV4 stereomicroscope was also used to capture the cantilevers, micro-size samples, and the observation of the saddle fracture pattern. MicroCT imaging was conducted using an inspeXio SMX-90CT Plus (Shimadzu, Japan) microCT machine using a 90 kV voltage and 0.012 mm/pix voxel size. The 3D models were then rendered using VGStudio Max software.

Nanoindentation: Stress-Strain Curves. Depending on the type of experiment, different modes of indentation were used using a Triboindenter TI-950 depth-sensing nanoindenter tester (Hysitron, Minneapolis, MN, USA). Hertzian contact studies were conducted on embedded and finely polished samples using a 30 mN load transducer and a cono-spherical fluid cell tip with 10 μm nominal radius. For each indentation cure on the outer and inner layers, 70 partial loading-unloading cycles were conducted in the load ranges 10 μN to 30 mN, and 50 μN to 30 mN, for hydrated and dry conditions, respectively. The loading rates ranged from of 0.5 to 300 $mN.s^{-1}$. Before each experiment, and in order to minimize thermal drift, the tip was engaged with the sample for 30 to 40 min. Details of the data analysis for the indentation stress-strain curves can be found elsewhere (ALAM et al., 2015).

NanoDMA. Nanoscale dynamic mechanical analysis (NanoDMA) of the samples were conducted using a dynamic testing module (nanoDMA transducer, Hysitron). A CMX control algorithm was used as an add-in to the nanoDMA in order to accurately measure the storage and loss moduli modulus (E' and E''), as well as the viscoelastic loss parameter tan δ using the Kelvin-Voigt model (FERRY, 1980). These parameters were continuously monitored as a function of the indentation contact depth by superimposing a small sinusoidal load on the

quasistatic load. The experiments were performed with a fluid cell cube corner tip at a maximum load of 1000 μN and a frequency of 220 Hz on well-polished samples in both dry and hydrated conditions. The tip was calibrated for the required contact depth using a standard fused quartz and single crystal Aluminium samples using standard procedures.

Miniature cantilever cutting by picosecond laser cutting. In order to cut micro-size cantilevers from the saddle with a high precision, an ultrashort picosecond (ps) laser cutting technique was used. To avoid the generation of any pre-loading as well as to minimize damage due to the cutting process, saddles were not dissected from the whole merus to avoid imposing any mechanical stresses to the saddle structure. Cutting was conducted through scanning of the laser beam with a galvanometer scanner. The ps laser (Time-Bandwidth DUETTO, Switzerland) has a wavelength of 1064nm, beam quality M2 of <1.3, pulse frequency of 50 kHz to 8.2 MHz, pulse duration of <12 ps, nominal output power of 10 W to 15 W. The saddle sample was mounted on an x-y translation stage. The laser pulses were focused on the outer layer of the saddle using a conventional focal lens with a focal length of 100 mm, which produced a focal spot about 25 μm. In order to eliminate or minimize any laser-induced thermal effect or damage to the saddle sample, the cutting parameters have been optimized and used at scanning speed of 200 mm/s, pulse energy of 18.92 μJ and 500 KHz in pulse repetition rate. Reference markers were produced on the screen and the machine was set for over 10 scanning passes per plane to cut the sample to completion. A higher number of passes with a lower laser energy allowed to minimize damage in the sample. Moreover, the samples were kept hydrated to further minimize mechanical and drying stresses and the heat affected zone in the sample. The resulting cantilever slices were ~1.8 mm long, 200 μm wide, and 150-230 μm thick depending on the cutting position on the saddle, and were carefully separated under a light microscope using surgical forceps. The cantilevers were then mounted and clamped in between two 2 mm thick glass slides edges

with superglue so at least 1.2 mm of the miniature cantilever is out for micro-bending test as illustrated in Figure S4D.

Cantilever Bending. The same triboindenter mechanical tester equipped with a customised 350 μm stainless steel spherical tip (Figure S9) and a high load transducer (with a maximum force up to 10 N) (Hysitron, MN, USA) were used to bend the cantilevers and extract the force versus deflection curves.

Tensile testing. A custom-made micro uniaxial testing machine was used (Figure S10) to analyse the inner layer strips under tensile loading. The micro-testing machine was designed to conduct experiments in both dry and hydrated conditions. The load and displacement are monitored using a LSB200 load cell (FUTEK, USA) and a Linear Variable Displacement Transducer (LVDT) (S series, Solartron, UK) with 0.1 N force and 1 μm displacement resolutions, respectively. The load cell and LVDT were calibrated before the experiments. SENSIT test and measurement software (Futek, USA) was used to record the load-displacement data. The load cell and LVDT were calibrated by their respective manufacturers. Hydrated strips of the inner layer were longitudinally fixed between the washers with very small drops of a superglue gel at the extremities of the strips and far ahead from the strained regions in order to avoid artefact from glue drying. The load was increased gradually at a rate of ~2.5 mN/s and the immersed samples were loaded until failure. The linear part of the load-displacement curves was used to calculate the Young's modulus of the samples. The width and length of each strip were measured using using a 1 μm resolution digital micrometer (series 293-230 Mitutoyo, Japan), with the data recorded on the computer using a USB-ITN cable (Mitutoyo, Japan). Sample that broke within the gripping area were removed from the data analysis.

Tensile samples. Strips for the tensile test were obtained by initially removing the outer layer by treating whole saddles in an 0.1 M EDTA solution for 7 days. The resulting softer demineralized saddles, devoid of the outer layer, were cut into longitudinal thin strips 0.5 to 0.9 mm wide with a surgery scalpel under a Zeiss Stemi DV4 stereomicroscope. The width, length, and thickness of each strip were measured using 1 μm resolution digital micrometer (series 293-230 Mitutoyo, Japan). These strips were kept hydrated all the time during demineralization, cutting, and later during tensile testing.

In order to quantify the role of elastic proteins on the inner later tensile response, some demineralized samples were further soaked in an alkaline peroxide solution (mixture of H_2O, 30% H_2O_2, and 10N NaOH, with volume pct. of 92.5%, 5%, 2.5%, respectively) at 70° C until the samples were completely de-proteinized, according to a procedure described in Ref. (MISEREZ et al., 2008). The resulting strips, which were only composed of chitin as verified by Fourier Transform Infrared Spectroscopy (FTIR) and amino acid analysis (AAA) (TADAYON et al., 2015), were fixed between washers and were subjected to tensile loading under hydrated conditions.

In order to assess the differences in protein composition in the outer and inner layers, a small amount of each layer were separated and soaked in alkaline peroxide to selectively dissolve the proteins (but not the chitin). The alkaline supernatant containing the proteins was then acid-hydrolysed in 6M HCl with 5% phenol as an anti-oxidant *in vacuo*. The hydrolysates were flash-evaporated using a speed vacuum (Scan Speed, USA), and were then washed twice with water and methanol. The proteins were re-suspended in 300 μl of Sample Dilution Buffer (SYKAM, Germany). The hydrolysis was performed at 110° C for 24 hours. AAA was conducted using a Ninhydrin-based, post-column derivatization Sykam S 433 AAA. The elution time of the peaks was calibrated using a standard amino acid solution provided by the manufacturer.

Finite Element Modelling (FEM). FEM was carried out to visualize the stress profile in the outer and inner layer and quantify the maximum compressive and tensile stresses using SolidWorks. Considering the saddle as a double ruled surface shape, we used two parabola curves to fit the two opposite extracted curves from two main cross sectional planes (sagittal and transverse) of the sample at the saddle point (Figures S5A,B). An average thickness of 26 saddles were used to specify the thickness of the curves into surfaces. We constructed the 3D simplified model using the "Loft" command to slide a parabola on the other one. The extra parts at the sides and corners were cut to give the same shape of the mantis shrimp saddle to the 3D model. We avoided any sharp corners to avoid any stress localizations in the edges and as it was in real saddle. The two parts of the outer and inner layers were defined based on the real samples thickness and spatial geometry. For each part a linear elastic isotropic material was assumed and the mechanical and physical properties of the layers (E_{IL}=900 MPa, E_{OL}=10 GPa) as well as extracted physical properties of the layers (density ρ_{IL} = 1.5 g/cm^3, ρ_{0L} = 2.5 g/cm^3; and Poisson ratio ν_{IL} = 0.30, ν_{0L} = 0.25) was used to define the materials specifications. Due to the symmetrical shape and loading regime of the model, we defined a mirror symmetry feature in the transversal cross-section at the saddle point and a *z*-direction confinement is applied. Since, no delamination ever observed in the saddle structure even under excessive compression loadings in our previous study (TADAYON et al., 2015), the global contact in the layers interface was assumed to be fully-bonded and ideal. The model was restricted from both sides in sagittal plane. A static direct transfer remote load of 20 N was applied to the sample from two points 0.5 mm from the contact region in transverse plane. We chose solid and standard 4-point mesh, 50 μm size with 2.5 μm tolerance, resulting in 1014293 nodes and 705923 elements. Subsequently the degree of freedom (DOF) was 3042081. Analysis type was chosen to be static.

Data analysis and plotting. The parabola curve fitting used to construct the 3D model of the saddle and data plotting were done using OriginPro 9.1 software. Statplus software was used for the statistical analysis. A total number of 28 saddle samples were used and tested in the entire study. All samples were collected from fresh mantis shrimps with fully-formed outer and inner layers.

References

Alam, P., Fagerlund, P., Hägerstrand, P., Töyrylä, J., Amini, S., Tadayon, M., Miserez, A., Kumar, V., Pahlevan, M. & Toivakka, M. (2015). l-Lysine templated CaCO3 precipitated to flax develops flowery crystal structures that improve the mechanical properties of natural fibre reinforced composites. *Composites Part A: Applied Science and Manufacturing,* 75**,** 84-88.

Ferry, J. D. (1980). *Viscoelastic Properties of Polymers*, Wiley.

Miserez, A., Schneberk, T., Sun, C., Zok, F. W. & Waite, J. H. (2008). The Transition from Stiff to Compliant Materials in Squid Beak. *Science,* 319**,** 1816-1819.

Tadayon, M., Amini, S., Masic, A. & Miserez, A. (2015). The Mantis Shrimp Saddle: A Biological Spring Combining Stiffness and Flexibility. *Advanced Functional Materials,* 25**,** 6437-6447.